Spectrochimica Acta Part A 83 (2011) 398–405

Contents lists available at SciVerse ScienceDirect

Spectrochimica Acta Part A: Molecular and Biomolecular Spectroscopy

journal homepage: www.elsevier.com/locate/saa

Structural and fluorescence quenching characterization of hematite nanoparticles

Ahmed S. Al-Kady[a], M. Gaber[a], Mohamed M. Hussein[b], El-Zeiny M. Ebeid[a,c,*]

[a] Chemistry Department, Faculty of Science, Tanta University, Tanta, Egypt
[b] Faculty of Pharmacy, Cairo University, Cairo, Egypt
[c] Misr University for Science and Technology (MUST), 6th October City, Egypt

ARTICLE INFO

Article history:
Received 2 June 2011
Received in revised form 9 July 2011
Accepted 24 August 2011

Keywords:
Characterization
Hematite
Iron oxide nanoparticles
Coumarin thiourea
Fluorescence quenching
Static and dynamic quenching

ABSTRACT

Nanoparticles of the dominant hematite form (α-Fe_2O_3) of iron oxide have been prepared by a simple route of dropping $FeCl_3$ solution into boiling water. The nanoparticles have been characterized by transmission electron microscopy (TEM), UV–visible electronic absorption spectroscopy, chemical stoichiometry, thermal analysis methods (TGA, DSC and DTA), XRD, FTIR and magnetic susceptibility measurements. Kinetic analysis of the DSC calorigram of thermal dehydration of the nanoparticles reveals one stage of the dehydration process of energy of activation of 29.0 kJ mol^{-1}. The role of iron oxide nanoparticles in fluorescence quenching of coumarin thiourea derivatives (I–IV) was investigated at room temperature (296 K) by means of steady-state fluorescence spectroscopy. The quenching process was characterized by Stern–Volmer (S–V) plots which display a positive deviation from linearity. This could be explained by static and dynamic quenching models. The positive deviation in the S–V plot is interpreted in terms of ground-state complex formation model and sphere of action static quenching model. Various rate parameters for the fluorescence quenching process were determined by using the modified Stern–Volmer equation. The sphere of action static quenching model agrees very well with experimental results. Quenching constants for iron oxide nanoparticles are about four orders of magnitudes higher than quenching by Fe^{3+} ions.

1. Introduction

Nanoparticles of iron oxides and their suspensions have extensive applications in magnetic sealing, oscillation damping, position sensing [1] ultra high density magnetic storage media [2], clinical diagnosis and treatment [3], biological labeling, tracking, imaging, detection, and separations [4]. Their characteristics depend significantly on particle size, particle morphology and size distribution.

Hematite, the most stable iron oxide, is of scientific and technological importance as a catalyst, pigment, ion exchanger, magnetic material, lithium-ion battery component and gas sensor [5–9]. Hematite is an antiferromagnetic semiconductor, the color of which varies with particle size and aggregation form [10]. The electrical properties of hematite can be widely modified with some impurities [11]. Further, it is a starting material for the magnetic iron oxides used in magnetic recording tapes [12].

Some studies have been carried out on the preparation of monodisperse α-Fe_2O_3 particles using a two-step hydrolysis of dilute $FeCl_3$ aqueous solution [13]. The first step is the hydrolysis of $FeCl_3$ solution at 70–90 °C, which provided β-FeOOH colloidal suspension, and the second step is the transformation from β-FeOOH at 100–120 °C via a dissolution and recrystallization process. Partial neutralization with NaOH solution promotes the hydrolysis of highly concentrated $FeCl_3$ solutions. The particle size of α-Fe_2O_3 can be controlled by neutralization degree, and it decreases with decreasing the electrolyte concentration. Forced hydrolysis of Fe^{3+} solutions involves hydrolyzing Fe $(NO_3)_3$, Fe $(ClO_4)_3$ or $FeCl_3$ solutions at a temperature close to 100 °C under strongly acidic conditions. If hematite is prepared from Fe $(NO_3)_3$ or Fe $(ClO_4)_3$, it forms Fe^{3+} hydroxyl species [14], whereas, if hematite is prepared from $FeCl_3$, akaganeite may be an intermediate product which then transforms *in situ* to hematite [15]. Hematite production by transformation of ferrihydrite starts with the precipitation of ferrihydrite which is then converted into hematite in aqueous suspension by a short-range crystallization process within the ferrihydrite aggregates. This transformation takes place under weakly acid to weakly alkaline conditions and requires the presence of some water within the ferrihydrite aggregates [16].

The acicular hematite particles are formed as products of hydrothermal transformation of suspensions of amorphous iron (III) hydroxide in water at temperatures above 100 °C in an autoclave in the presence of chelating agents, e.g. citric acid, tartaric acid or 1-hydroxyethyl-1,1-diphosphonic acid [17]. The mechanical

* Corresponding author at: Chemistry Department, Faculty of Science, Tanta University, Tanta, Egypt. Tel.: +20 403318302; mobile: +20 107072725.
E-mail address: drzeiny@yahoo.com (E.-Z.M. Ebeid).

1386-1425/$ – see front matter © 2011 Elsevier B.V. All rights reserved.
doi:10.1016/j.saa.2011.08.052

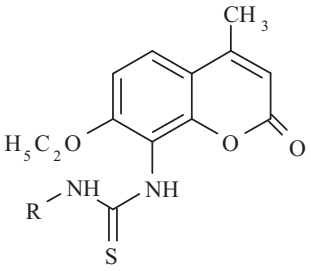

Coumarin	R
I	C_2H_5
II	C_3H_5
III	C_6H_5
IV	C_6H_{11}

Scheme 1. The molecular structure of coumarin thiourea derivatives (I–IV).

dehydration of γ-FeOOH leads to different products if the process is carried out by dry grinding (conversion to hematite) [18]. A thermally induced dehydration can either be a direct transformation from goethite to hematite [19,20], or a transformation with the formation of an intermittent super structure phase called protohematite or hydro hematite before formation of hematite [21–24].

A simple method was described [25] for the preparation of colloidal iron oxide by dropwise addition of $FeCl_3$ aqueous solution to boiling water. A reddish colloidal solution of hydrated iron oxide was obtained that is indefinitely stable. The ferric oxide particles thus prepared are surrounded by Fe^{3+} ions that hold the insoluble α-Fe_2O_3 particles in suspension. This explains the positive charge on the colloidal particles. The characterization of such colloidal system is useful due to its potential importance in various chemical and medical fields.

The fluorescence quenching of organic molecules including coumarin and its derivatives in solution by various quenchers like carbon tetrachloride, acetone, aromatic hydrocarbons, fullerene, aniline, aromatic amines, halide ions, methylene bromide, haloalkanes, chloromethane, etc. has been studied by several investigators [26–42] by steady-state and transient methods. The quenching of organic fluorophores by nanoparticles is thought to arise from dynamic quenching [43–45], both dynamic and static mechanisms are involved in the quenching [46–48]. The quenching mechanism is important not only in physical science, but also in chemical, biological, and medical sciences.

The general chemical structure of coumarins consists of a benzene moiety fused to α-pyrone rings and most of them have a very efficient fluorescing ability. Coumarin derivatives possess a wide range of applications as anticoagulants [49], antitumor agents [50], photosensitizers [51], anti-HIV agents [52], antimicrobial agents [53], chemosensors [54], and anti inflammatory agents [55]. Coumarin derivatives have been linked to other molecules in gene expression studies [56] as well as in salmonella detection [57]. Coumarin derivatives are also currently used as fluorogenic dyes in proteomics [58]. Due to the interesting properties associated with coumarins, we undertook the fluorescence studies of newly synthesized coumarin thiourea derivatives (Scheme 1). In the present study we have used steady state fluorescence to investigate quenching of coumarin thiourea derivatives (I–IV) by hydrated iron oxide nanoparticles to understand the nature of the quenching mechanism.

2. Experimental

2.1. Materials and instruments

The solute coumarin thiourea derivatives (I–IV) were freshly synthesized using standard method [59]. Iron chloride ($FeCl_3$, 99%) was purchased from Fluka. Methanol was purchased from Fluka. Poly (ethylene glycol) was obtained from Aldrich. Double-distilled water was used throughout this study.

Steady-state emission spectra were measured using a Shimadzu RF 510 spectrofluorophotometer connected to a Haake Ultrathermostat (Julabo F10) of temperature precision ±0.1 °C using a rectangular quartz cell of dimensions 0.2 cm × 1 cm to minimize the reabsorption. UV–vis absorption spectra were measured using a Shimadzu UV-160A spectrophotometer. Thermogravimetric analysis (TGA) was carried out under dynamic flow of nitrogen (30 ml/min) and a heating rate of 20 °C/min using a Shimadzu TGA-50 thermoanalyzer. DSC measurements were made in a nitrogen atmosphere (rate flow 30 ml/min) and heating rate of 10 °C/min using a Shimadzu DSC-50 Differential Scanning Calorimeter. Differential thermal analysis was carried out under dynamic flow of nitrogen gas (30 ml/min) and a heating rate of 10 °C/min up to 800 °C using a Shimadzu DTA-50. Simultaneous DTA–TGA runs were recorded using a Shimadzu DTG-60H apparatus. Kinetic analysis of the DSC calorigrams was conducted according to Thomas and Clarke [60]. X-ray diffraction analysis was carried out using a Philips PW 1390 X-ray diffractometer using copper target with Nickel filter. Each sample was subjected to X-ray analysis under working conditions of 40 kV and 20 mA. All the difractograms were investigated in the 2θ values in the range of 5–70° at room temperature. Fourier transform infrared (FTIR) spectroscopy was recorded on a Perkin-Elmer 1430 spectrophotometer in the range of 4000–400 cm^{-1}. The FTIR spectra were recorded at room temperature in KBr pellets. The nanoparticle size and morphology were analyzed either by a transmission electron microscope (TEM), JEOL-JEM 1230, operating at an accelerating voltage of 120 kV or a Philips CM20 electron microscope operating at an accelerating voltage of 200 kV. A drop from aqueous suspension of solution was deposited on a ground piece of mesoporous silica or amorphous carbon–copper grid and left to evaporate at room temperature. Magnetic susceptibility at room temperature has been measured using a Bartington susceptibility-meter MS2B equipped with a dual frequency sensor that accepted 10 cm^3 samples in standard plastic pots. The calibration sample is provided by the manufacturer, and is normally a sample containing small ferrite beads.

2.2. Experimental procedures

2.2.1. Synthesis of iron oxide nanoparticles

A solution of 0.1 M $FeCl_3$ (15 ml) was added drop by drop to 100 ml of vigorously stirred boiling distilled water. The color changed from yellow ($FeCl_3$ solution) to red and upon excess addition of 0.1 M $FeCl_3$ the color turned to dark red. The resulting solution was heated to reflux and kept at that temperature for 30 min. The solution was then cooled to room temperature. Such colloidal solution can exist indefinitely without signs of precipitation. However, a reddish-brown precipitate was obtained upon dropping concentrated solution of sodium hydroxide.

2.2.2. Titrimetry of hematite

Accurately weighed amount (100 mg) of hematite was dissolved in 3 ml conc. HCl, diluted to 50 ml with distilled water. The pH of the solution was adjusted to 2–3 with a solution of NaOH, five drops of thiocyanate indicator where added (thiocyanate ion gives a red to colorless end point). The solution was titrated against 0.05 M

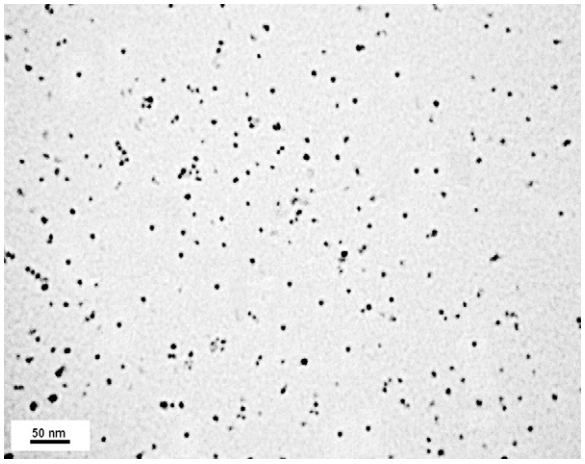

Fig. 1. TEM photograph of iron oxide nanoparticles.

ethylenediamine tetraacetic acid; EDTA solution (1.86 g/100 ml water). Each 1 ml of 0.05 M EDTA is equivalent to 2.793 mg Fe^{3+}.

2.2.3. Iron oxide nanoparticles as fluorescence quencher

The quenching of coumarin thiourea derivatives (I–IV) was studied using iron oxide nanoparticles as quencher. 1 ml of 5×10^{-5} M coumarin thiourea solution was mixed with the appropriate volume of iron oxide nanoparticles solution as quencher and the solution was made to the mark with methanol in 10 ml volumetric flasks.

3. Results and discussion

3.1. Characterization of iron oxide nanoparticles

3.1.1. Transmission electron microscopy (TEM)

The particle size and morphology were analyzed by transmission electron microscopy (TEM). Fig. 1 shows the TEM image of iron oxide nanoparticles that confirms the nanoscale dimension of the prepared particles and shows that the particles have an average diameter of about 6 nm.

3.1.2. UV–vis electronic absorption spectroscopy

Fig. 2 shows the absorption spectrum of different concentrations of a 6 nm diameter iron oxide nanoparticles aqueous solutions. The spectra show a characteristic absorption band centered at ca. 405 nm.

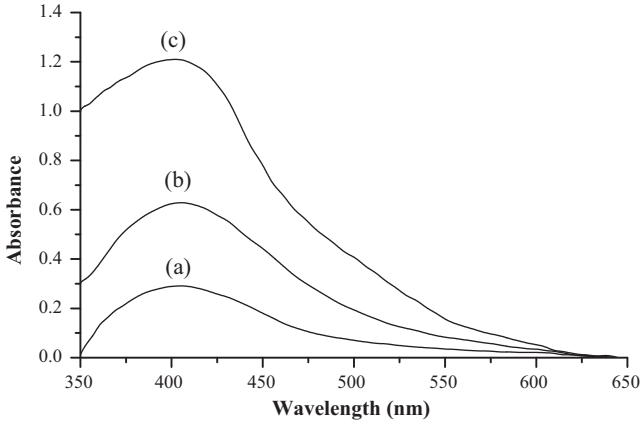

Fig. 2. Absorption spectra of iron oxide nanoparticles aqueous solutions of concentrations (a) 4.2, (b) 9.2 and (c) 17.7 nM.

Table 1
Stoichiometric analysis of iron oxide nanoparticles.

Iron oxide sample	End point (ml)	Weight of Fe^{3+} (mg)	% Fe^{3+}
Dried at room temperature	18.8	52.5	52.5
	17.0	47.5	47.5
	18.1	50.3	50.3
	16.0	44.7	44.7
Dried at 160 °C for 1 h	25.0	69.8	69.8
	24.9	69.6	69.6
	24.9	69.6	69.6
	24.8	69.3	69.3

3.1.3. Titrimetry studies

The titrimetry of iron oxide product was determined by chemical estimation of Fe^{3+} using EDTA. The data of four different batches of hematite samples dried at room temperature and at 160 °C for 1 h are shown in Table 1. Samples dried at room temperature show varying percentages of Fe^{3+} due to variation in concentration of water of hydration. Samples dried at 160 °C, show a constant percentage of iron at about 69.6%. This value is nearly the same as the theoretical percentage of iron in hematite; α-Fe_2O_3 of 70%.

3.1.4. Thermoanalytical techniques

Fig. 3a shows the differential scanning thermogram of iron oxide nanoparticles dried at room temperature. A single endothermic peak starting from room temperature up to 200 °C is obtained from which Arrhenius plot was constructed (Fig. 3d). Kinetic analysis of the DSC thermogram reveals one stage of the dehydration process of energy of activation of 29.0 kJ mol^{-1} (Table 2). As-prepared sample heated up to 160 °C in a DSC pan does not show an endothermic peak when rescanned immediately (Fig. 3b) but shows an endothermic peak when rescanned after leaving for 24 h in ambient atmosphere (Fig. 3c). During this time the sample is believed to absorb water from atmosphere. The enthalpy of activation ($\Delta H^{\#}$), free energy of activation ($\Delta G^{\#}$) and entropy of activation ($\Delta S^{\#}$) of the dehydration process were determined from Eyring's equation (1) and presented in Table 2.

$$\ln\left(\frac{k}{T}\right) = \ln\left(\frac{k_B}{h}\right) + \frac{\Delta S^{\#}}{R} - \frac{\Delta H^{\#}}{R}\frac{1}{T} \quad (1)$$

where k is the reaction rate constant, T is the absolute temperature, $\Delta H^{\#}$ is the enthalpy of activation, R is the gas constant, k_B is the Boltzmann constant, h is the Planck's constant and $\Delta S^{\#}$ is the entropy of activation. The plot of $\ln k/T$ versus $1/T$ gives a straight line with slope $-\Delta H^{\#}/R$ from which the enthalpy of activation can be derived and with intercept $\ln k_B/h + \Delta S^{\#}/R$ from which the entropy of activation is derived.

It is interesting to note that E_a values are higher than those for diffusion-controlled reactions (10–21 kJ mol^{-1}) [61]. Therefore, they are characteristic of a chemical reaction rather than a diffusion controlled process. Further scrutiny of Table 2 reveals consistent large and negative values for entropies of activation ($\Delta S^{\#}$). This implies a highly ordered transition state (i.e. tight transition state) in the course of the dehydration process.

The two proposed dehydration stages are clearly shown by derivative thermogravimetric (DrTGA) curves. A total mass loss of about 7% was observed and this loss is predominantly in the temperature range 40 and 140 °C and a negligibly small (<1%) mass loss was observed when heated to 600 °C. The observed mass loss is due to loss of water of hydration of iron oxide nanoparticles (Fig. 4). Differential thermal analysis (DTA) curves show two endothermic peaks in the temperature range 25–125 °C (Fig. 5).

3.1.5. X-ray diffraction (XRD) patterns

The phase and purity of the synthesized iron oxide nanoparticles were examined by X-ray diffraction technique. Fig. 6 shows

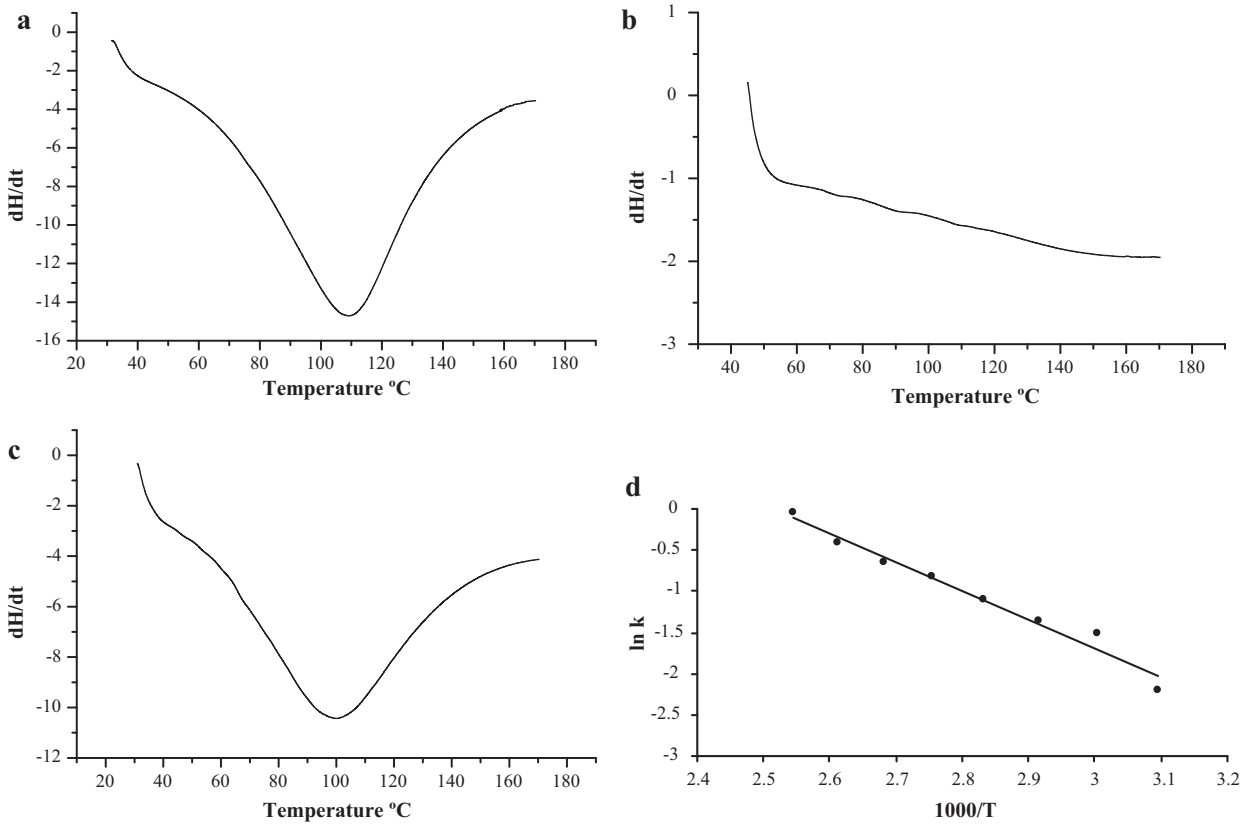

Fig. 3. (a) Differential scanning thermogram of as-prepared iron oxide nanoparticles dried at room temperature. (b) Differential scanning thermogram of iron oxide nanoparticles dried at 160 °C and rescanned immediately. (c) Differential scanning thermogram of iron oxide nanoparticles dried at 160 °C and rescanned after waiting for 24 h. (d) Arrhenius plot extracted from differential scanning thermogram of iron oxide nanoparticles dried at room temperature.

Table 2
Activation parameters extracted from differential scanning thermograms of as-prepared iron oxide nanoparticles.

Sample	E_a (kJ mol^{-1})	$\Delta H^{\#}$ (kJ mol^{-1})	$\Delta G^{\#}$ (kJ mol^{-1})	$\Delta S^{\#}$ (J/mol K)	Correlation coefficient (r)	Standard deviation (SD)
As-prepared samples dried at room temperature	29.0	26.25	84.61	−179.80	0.99807	0.07787

XRD pattern of iron oxide nanoparticles dried at room temperature. The peaks at $2\theta = 32^\circ$, 35°, 40° and 50° are due to hematite dominant phase [22,24,62]. Some of the intense peaks with hkl planes 012, 104, 110, 113, 024 and 116 of hematite was compared and matched well with the data reported by Schwertmann [14]. All the peaks can be readily indexed to hexagonal phase of α-Fe_2O_3. No other phase was observed in the synthesized iron oxide nanoparticles, which indicates the high purity of the sample.

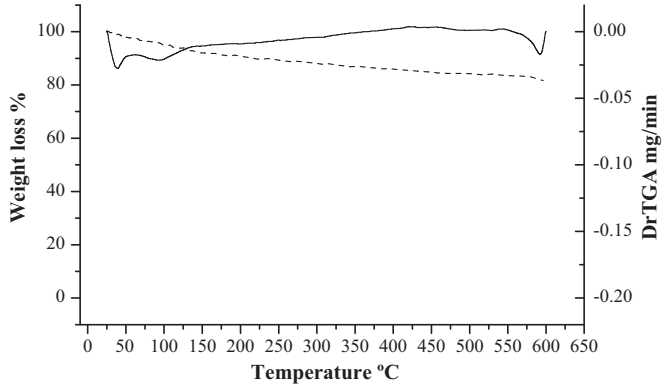

Fig. 4. TGA thermogram of as-prepared iron oxide nanoparticles (···) TGA and (—) DrTGA curves.

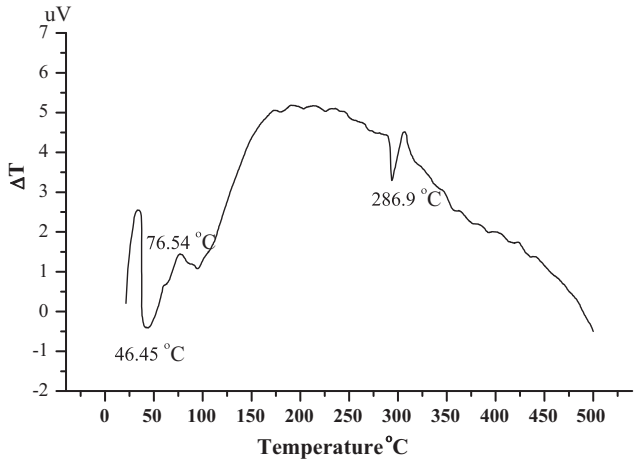

Fig. 5. DTA thermogram of as-prepared iron oxide nanoparticles.

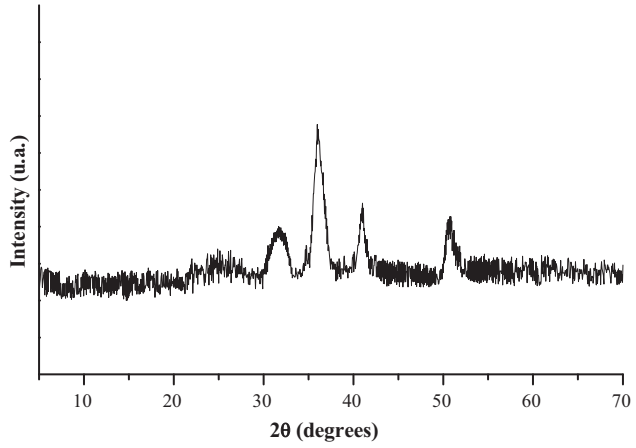

Fig. 6. XRD patterns of iron oxide nanoparticles.

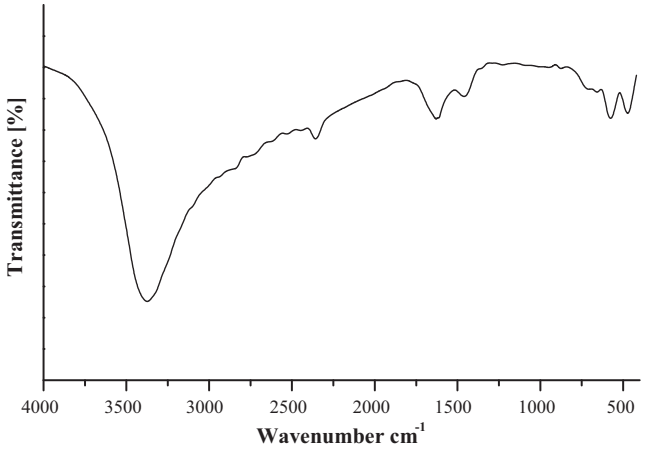

Fig. 7. FTIR spectrum of iron oxide nanoparticles.

3.1.6. Fourier transform infrared (FTIR) spectrophotometry

The FTIR spectrum of as-prepared iron oxide nanoparticles is shown in Fig. 7, which confirms the high purity of the sample. The main characteristic peaks of iron oxide nanoparticles are assigned in Table 3. The band at 3420 cm^{-1} is assigned to adsorbed water which also gives rise to the stretching mode of hydroxyl at 3217 cm^{-1} and the bending mode of hydroxyl at 1640 cm^{-1}. Other bands are as follows: 630 cm^{-1} and 570 cm^{-1} for Fe–O stretching mode of hematite and 468 cm^{-1} for lattice mode of FeO_6 [63,64].

3.1.7. Magnetic susceptibility

Magnetic susceptibility (χ) of iron oxide at room temperature was measured as $\chi = 103 \times 10^{-5}$ m^3 kg^{-1} indicating ferromagnetic properties of the synthesized iron oxide nanoparticles.

3.1.8. Lyophilization of iron oxide nanoparticles

When the aqueous solution of iron oxide nanoparticles was lyophilized, it gave an extremely deliquescent product that turns from solid into a syrup fluid once the vacuum in the lyophilizer is released and air access is allowed.

Table 3
FTIR band assignment for iron oxide nanoparticles.

Wavenumber (cm^{-1})	Assignment
3420	ν (H–O–H)
3217	ν (O–H)
1640	δ_{bend} –OH
630, 570	Fe–O stretching (ν_{Fe-O}) mode of hematite
468	FeO_6 lattice

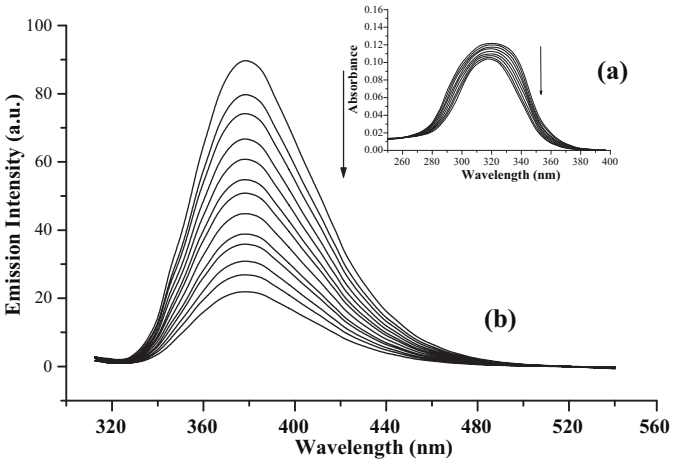

Fig. 8. Absorption (a) and emission (b) spectra (λ_{ex} = 330 nm) of 5×10^{-6} M of sample I in methanol/water (1:1) by volume recorded in the presence of iron oxide nanoparticles of concentrations (at decreasing intensities) as 0.00, 0.16, 0.32, 0.49, 0.65, 0.81, 0.97, 1.14, 1.30, 1.46, 1.62, 1.79 and 1.94 nM.

3.2. Fluorescence quenching studies

Fig. 8 shows the quenching fluorescence spectra of coumarin thiourea derivative I in the presence of variable concentrations of iron oxide nanoparticles in methanol/water (1:1) by volume. The fluorescence emission of sample I exhibits maximum at 376 nm upon excitation at 330 nm. The following observations were made: (i) the shape and band maxima of absorption and fluorescence spectra remain unchanged, (ii) no other emission band of the fluorophore towards red is noticed and (iii) absorbance of the fluorophore does not change during the course of the experiment.

The above observations suggest that (i) the fluorophore–quencher interaction does not change the absorption and fluorescence spectral properties, (ii) the formation of any emissive exciplex may be discounted, and (iii) there is no observable photochemical reaction between fluorophore and quencher. Similar behavior is displayed by coumarin thiourea derivatives (II–IV) with variable concentrations of iron oxide nanoparticles.

The dynamic process in which quenching mechanism is mainly due to collision is governed by the linear Stern–Volmer equation [65]:

$$\frac{I_0}{I} = 1 + K_{SV}[Q] \quad (2)$$

where I_0 and I are steady state fluorescence intensities in the absence and presence of quencher, respectively; K_{SV} is the Stern–Volmer quenching constant and [Q] is the concentration of quencher. The Stern–Volmer plots obtained by using experimentally determined values of I_0 and I are found to be nonlinear showing positive deviation and are shown in Fig. 9. Similar experimental results were also observed by others [31,66–69]. The positive deviation from linearity suggests that the quenching is not purely dynamic, and hence it may be due to the simultaneous presence of dynamic and static quenching.

In order to see whether ground-state complex is partly/purely playing a role, one can use the extended S–V equation [70] as

$$\frac{I_0}{I} = 1 + (K_{SV} + K_g)[Q] + (K_{SV}K_g)[Q]^2$$

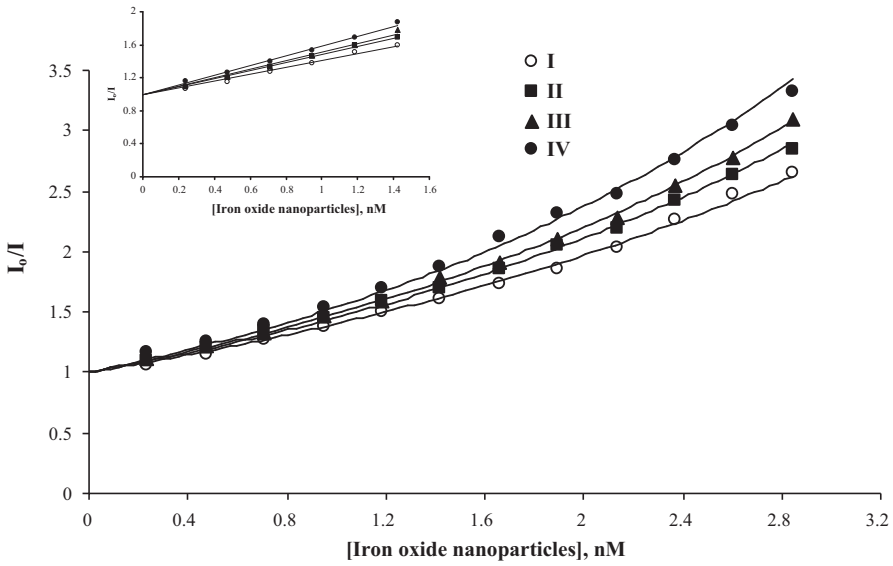

Fig. 9. Stern–Volmer plots I_0/I versus [Q] of the quenching of 5×10^{-6} M of coumarin thiourea derivatives (I–IV) by iron oxide nanoparticles in methanol/water (1:1) by volume of concentrations (at decreasing intensities) as 0.00, 0.16, 0.32, 0.49, 0.65, 0.81, 0.97, 1.14, 1.30, 1.46, 1.62, 1.79 and 1.94 nM. The fluorescence intensities were monitored at 376 nm, λ_{ex} = 330 nm. (Inset) Linear portions of Stern–Volmer plots.

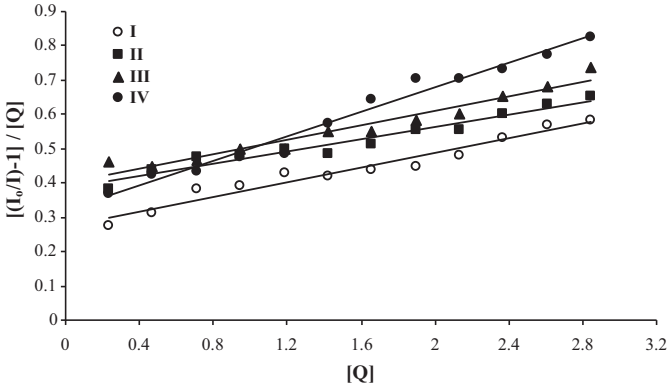

Fig. 10. The plots of $[I_0/I - 1]/[Q]$ versus [Q] for coumarin thiourea derivatives (I–IV) in methanol/water (1:1) by volume.

or

$$\frac{[I_0/I - 1]}{[Q]} = (K_{SV} + K_g) + (K_{SV}K_g)[Q] \quad (3)$$

where K_{SV} and K_g are the dynamic/(S–V) quenching constant and ground-state association constant of the complex, respectively. Our experimental data are fitted to Eq. (3), and using least-square fit procedure, K_{SV} and K_g have been determined. Fig. 10 shows the plots of $[I_0/I - 1]/[Q]$ versus [Q], which are straight lines with intercept ($K_{SV} + K_g$) and slope ($K_{SV}K_g$). These plots are linear with correlation coefficient nearly equal to unity. This indicates the quenching is not purely dynamic, and hence it may be due to the simultaneous presence of dynamic and static quenching. The individual values of K_{SV} and K_g calculated from the values of intercepts and slopes were presented in Table 4. From Table 4 one can see that the value of K_g is much smaller than K_{SV}. The dynamic quenching constant obtained do not agree well with that obtained from the lower portion of the S–V plot according to Eq. (2), i.e. in the low concentration region in the plot of I_0/I versus [Q], which is nearly linear. Apart from this, there is no shift in the band maxima of the absorption and emission spectra with different quencher concentrations as shown in Fig. 8a. Hence, the positive deviation due to ground-state complex formation is discarded in the present case [36,37]. Hence, the analysis of the data was carried out by employing the sphere of action static quenching model.

According to this model static quenching occurs if the quencher molecule is very near to, or, is in contact with the fluorophore at the exact moment it happens to be excited. This was explained by the fact that only a certain fraction W of the excited state is actually quenched by the collisional mechanism. Some molecules in the excited state, the fraction of which is $(1 - W)$, are deactivated almost instantaneously after being formed; because a quencher molecule happens to be randomly positioned in the proximity at the time the molecules are excited and interacts very strongly with them.

Table 4
Quenching parameters of coumarin thiourea derivatives (I–IV) by iron oxide nanoparticles at room temperature.

Coumarin	K_{SV} [a] $\times 10^8$ (M^{-1})	K_{SV} [b] $\times 10^8$ (M^{-1})	K_g [c] $\times 10^8$ (M^{-1})	K_{SV} [d] $\times 10^8$ (M^{-1})	V[e] $\times 10^8$ (M^{-1})	R_Y (Å)	$R_Y + R_Q$ (Å)	r[f] (nm)
I	9.64	6.61	2.61	6.58	2.45	4.97	34.97	585.43
II	8.59	5.89	2.06	5.95	1.76	5.38	35.38	576.31
III	8.44	5.77	1.87	5.87	1.75	5.72	35.72	574.90
IV	8.41	5.70	1.71	5.83	1.71	5.78	35.78	564.27

R_Q = 30 Å.

[a] S–V quenching constant (dynamic quenching constant) determined (lower concentration of the S–V plot) from Eq. (2).
[b] S–V quenching constant (dynamic quenching constant) determined from Eq. (3).
[c] Ground-state association constant of the complex determined from Eq. (3).
[d] S–V quenching constant (dynamic quenching constant) determined from Eq. (7).
[e] Static quenching constant determined from Eq. (5).
[f] Radius of sphere of action called as kinetic distance determined from Eq. (6).

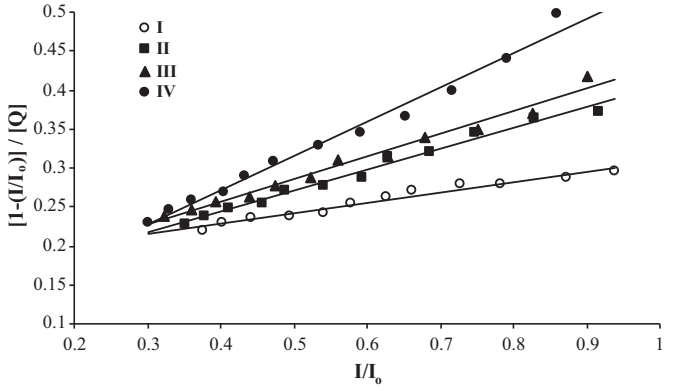

Fig. 11. The plots of $[1-(I/I_0)]/[Q]$ versus (I/I_0) for coumarin thiourea derivatives (I–IV) in methanol/water (1:1) by volume.

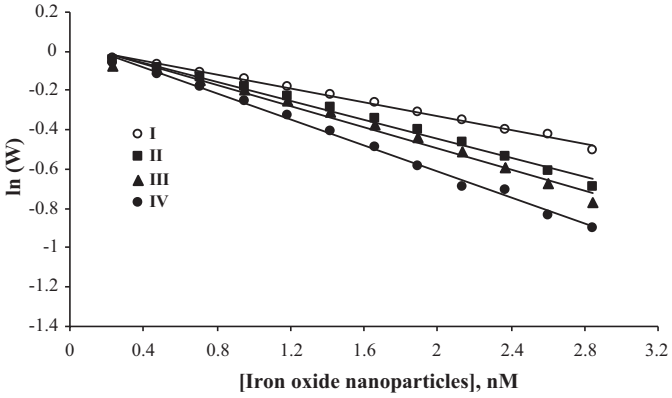

Fig. 12. The plots of ln (W) versus $[Q]$ for coumarin thiourea derivatives (I–IV) in methanol/water (1:1) by volume.

Numerous quenching models [65,71–73] have been produced to understand the static or instantaneous quenching process on the basis of modified form of the Stern–Volmer equation given as:

$$\frac{I_0}{I} = \frac{1 + K_{SV}[Q]}{W} \tag{4}$$

The additional factor W is expressed as:

$$W = e^{-V[Q]} \tag{5}$$

where V is the static quenching constant and it represents an active volume element surrounding the fluorophore in its excited state.

Frank and Wawilow [73] suggested that the static or instantaneous quenching occurs in a randomly distributed system when a quencher happens to reside within a sphere of action surrounding a fluorophore upon its excitation, the volume of such of action is given by:

$$\frac{V}{N'} = \frac{4}{3}\pi r^3 \tag{6}$$

where N' is Avogadro's number and r the radius of sphere of action called as kinetic distance. As W depends on the quencher concentration $[Q]$, the S–V plots for a quencher with high quenching ability generally deviate from linearity. Thus, it is worth rewriting Eq. (4) as

$$\frac{[1-(I/I_0)]}{[Q]} = K_{SV}\left(\frac{I}{I_0}\right) + \frac{1-W}{[Q]} \tag{7}$$

According to Eq. (7), $(1-I/I_0)/[Q]$ was plotted against I/I_0 and the S–V quenching constant, K_{SV} was obtained by the least-square fit method determining the slope. The intercept of the plot was used to calculate the W values for each quencher concentration $[Q]$. From the W values, the static quencher constant V was obtained using Eq. (5). Both procedures are illustrated in Figs. 11 and 12. From the V values the effective quenching radii were estimated. The results are reported in Table 4.

The radii of the solute (R_Y) and the quencher (R_Q) molecules were determined by using the additive model of Edward [74] and are given in Table 4. From these values of R_Y and R_Q, the sum of the molecular radii, i.e. encounter distance $(R = R_Y + R_Q)$ is determined. From Table 4, we see that the values of kinetic distance 'r' are greater than the encounter distance R. Therefore, according to Andre et al. [75] and Zeng and Durocher [40], the static effect takes place irrespective of the ground state complex formation provided the reactions are limited by diffusion indicating the sphere of action model holds well. Further, it may also be noted that a positive deviation in S–V plot is expected when both static and dynamic quenching occur simultaneously [66]. The dynamic quenching component is larger when compared to the static component. The above results suggest that the positive deviation in

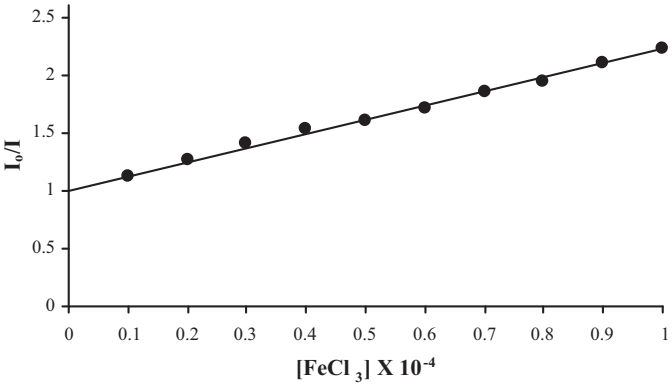

Fig. 13. Stern–Volmer plot I_0/I versus $[Q]$ of the quenching of 1×10^{-5} M of sample I by Fe^{3+} metal ion in methanol/water (1:1) by volume (at decreasing intensities) as 0.00, 0.1, 0.2, 0.3, 0.4, 0.5, 0.6, 0.7, 0.8, 0.9 and 1×10^{-4} M. The fluorescence intensities were monitored at 376 nm, λ_{ex} = 330 nm.

S–V plots is due to the presence of a small static quenching component in the overall dynamic quenching. It is also found that the quenching efficiences of iron oxide nanoparticles increase as R_Y of coumarins decreases.

The quenching of sample (I) was studied using Fe^{3+} ion as quencher. S–V plot (Fig. 13) gives S–V quenching constant K_{SV} of $1.22 \times 10^4\ M^{-1}$. The values of S–V quenching constants for iron oxide nanoparticles (Table 4) are more than four orders of magnitudes higher than quenching by Fe^{3+} ion. The fact that smaller particles of iron oxide nanoparticles are efficient quenchers of molecular fluorescence is an important finding and this is due to higher surface to bulk atom ratio of the smaller particles. As, the fluorescence intensity is related to the concentration of the quencher. Therefore, the quenched fluorophore can serve as an indicator for quenching agent.

4. Conclusion

In this study, iron oxide nanoparticles were prepared by a simple route of dropping $FeCl_3$ solution into boiling water. The resulting nanoparticles were characterized by TEM, UV–vis electronic absorption spectroscopy, chemical stoichiometry, thermal analysis methods (TGA, DSC and DTA), XRD, FTIR and magnetic susceptibility measurements. The quenching mechanism of coumarin thiourea derivatives with iron oxide nanoparticles was also discussed. The S–V plots show positive deviation indicating efficient fluorescence quenching. The positive deviation from linearity suggests that the quenching is due to the simultaneous presence

of dynamic and static quenching. As a result of the remarkable quenching of the fluorescence intensity of coumarin thiourea derivatives in the presence of iron oxide nanoparticles, it is possible for coumarin thiourea derivatives to directly sense and detect iron oxide nanoparticles by fluorescence intensity.

References

[1] K. Raj, R. Moskowitz, J. Magn. Magn. Mater. 85 (1990) 233–245.
[2] H. Zeng, J. Li, J.P. Liu, Z.L. Wang, S.H. Sun, Nature 420 (2002) 395–398.
[3] A. Jordan, R. Scholz, K. Maier-Hauff, M. Johannsen, P. Wust, J. Nadobny, H. Schirra, H. Schmidt, S. Deger, S. Loening, W. Lanksch, R. Felix, J. Magn. Magn. Mater. 225 (2001) 118–126.
[4] (a) J.W. Bulte, T. Douglas, B. Witwer, S.C. Zhang, E. Strable, B.K. Lewis, H. Zywicke, B. Miller, P.V. Gelderen, B.M. Moskowitz, L.D. Duncan, J.A. Frank, Nat. Biotechnol. 19 (2001) 1141–1147;
(b) J.M. Nam, C.S. Thaxton, C.A. Mirkin, Science 301 (2003) 1884–1886.
[5] T. Cheng, Z.Y. Fang, Q.X. Hu, K.D. Han, X.Z. Yang, Y.J. Zhang, Catal. Commun. 8 (2007) 1167–1171.
[6] F. Bondioli, A.M. Ferrari, C. Leonelli, T. Manfredini, Mater. Res. Bull. 33 (1998) 723–729.
[7] S. Mitra, S. Das, K. Mandal, S. Chaudhuri, Nanotechnology 18 (2007) 275608.
[8] J. Chen, L.N. Xu, W.Y. Li, Adv. Mater. 17 (2005) 582–586.
[9] Y. Wang, S.R. Wang, Y.Q. Zhao, B.L. Zhu, F.H. Kong, D. Wang, S.H. Wu, W.P. Huang, S.M. Zhang, Sens. Actuators B 125 (2007) 79–84.
[10] T. Takada, J. Jpn. Soc. Powder Powder Metall. 4 (1958) 120–168.
[11] K.H. Kim, S.H. Lee, J.S. Choi, J. Phys. Chem. Solids 46 (1985) 331–338.
[12] A.R. Corradi, S.J. Andress, J.E. French, G. Bottoni, D. Candolfo, A. Cechetti, F. Masoli, IEEE Trans. Magn. 20 (1984) 33–38.
[13] T. Nakamura, H. Kurokawa, J. Mater. Sci. 30 (1995) 4710–4714.
[14] (a) J.H. Johnston, D.G. Lewis, Geochim. Cosmochim. Acta 47 (1983) 1823–1831;
(b) U. Schwertmann, R.M. Cornel, Iron Oxide in the Laboratory: Preparation and Characterization, 2nd ed., Wiley, New York, 2000.
[15] S. Hamada, E. Matijevic, J. Colloid Interface Sci. 84 (1981) 274–277.
[16] U. Schwertmann, J. Friedl, H. Stanjek, J. Colloid Interface Sci. 209 (1999) 215–223.
[17] V. Arndt, IEEE Trans. Magn. 24 (1988), 1798–1798.
[18] D. Klissurski, V. Blaskov, J. Chem. Soc. Chem. Commun. (1983) 863–864.
[19] D. Walter, G. Buxbaum, W. Laqua, J. Therm. Anal. Calorim. 63 (2001) 733–748.
[20] F. Watari, P. Delavignette, S. Amelinckx, J. Solid State Chem. 29 (1979) 417–427.
[21] E. Wolska, Z. Kristallogr. 154 (1981) 69–75.
[22] E. Wolska, Solid State Ionics 28 (1988) 1349–1351.
[23] E. Wolska, U. Schwertmann, Z. Kristallogr. 189 (1989) 223–237.
[24] A.F. Gualtieri, P. Venturelli, Am. Mineral. 84 (1999) 895–904.
[25] (a) J.E. Brady, G.E. Humiston, General Chemistry: Principles and Structure, John Wiley & Sons, New York, 1986, p. 392;
(b) C.H. Sorum, J. Am. Chem. Soc. 50 (1928) 1263–1267.
[26] D.S. Biradar, J. Thipperudrappa, S.M. Hanagodimath, Spectrosc. Lett. 40 (2007) 559–571.
[27] V.K. Sharma, D. Mohan, P.D. Sahare, Spectrochim. Acta A 66 (2007) 111–113.
[28] H. Pal, D.K. Palit, J.P. Mittal, J. Chem. Soc. Faraday Trans. 89 (1993) 683–691.
[29] K. Datta, A.K. Mukharjee, Spectrochim. Acta A 65 (2006) 261–264.
[30] T.P. Giraddi, J.S. Kadadevaramath, G.H. Malimath, G.C. Chikkur, Appl. Radiat. Isot. 47 (1996) 461–466.
[31] B.G. Evale, S.M. Hanagodimath, J. Lumin. 130 (2010) 1330–1337.
[32] S. Nad, H. Pal, J. Phys. Chem. A 104 (2000) 380–673.
[33] A. Chakraborty, D. Chakraborty, D. Seth, P. Hazra, N. Sarkar, Spectrochim. Acta A 63 (2006) 594–602.
[34] A.C. Tablet, M. Hildebrand, J. Photochem. Photobiol. A: Chem. 189 (2007) 73–79.
[35] A.K. Satpati, S. Nath, M. Kumbaharkar, D.K. Maity, S. Senthikumar, H. Pal, J. Mol. Struct. 878 (2008) 84–94.
[36] P.K. Behera, T. Mukherjee, A.K. Mishra, J. Lumin. 65 (1995) 131–136.
[37] D.S. Biradar, J. Thipperudrappa, S.M. Hanagodimath, J. Lumin. 126 (2007) 339–346.
[38] M. Swaminathan, N. Radha, Spectrochim. Acta A 60 (2004) 1839–1843.
[39] R. Giri, Spectrochim. Acta A 60 (2004) 757–763.
[40] H. Zeng, G. Durocher, J. Lumin. 63 (1995) 75–84.
[41] C. Hariharan, A.K. Mishra, Radiat. Meas. 32 (2000) 113–121.
[42] S.K. Saha, S.K. Dogra, J. Lumin. 75 (1997) 117–125.
[43] A. Kotiaho, R. Lahtinen, H. Latvala, A. Efimov, N.V. Tkachenko, H. Lemmetyinen, Chem. Phys. Lett. 471 (2009) 269–275.
[44] S. Pramanik, S.C. Bhattacharya, T. Imae, J. Lumin. 126 (2007) 155–159.
[45] C.F. Landes, M. Braun, M.A. El-Sayed, J. Phys. Chem. B 105 (2001) 10554–10558.
[46] I.S. Lee, H. Suzuki, J. Photochem. Photobiol. A: Chem. 195 (2008) 254–260.
[47] S.K. Ghosh, A. Pal, S. Kundu, S. Nath, T. Pal, Chem. Phys. Lett. 395 (2004) 366–372.
[48] T. Huang, R.W. Murray, Langmuir 18 (2002) 7077–7081.
[49] J. Lowenthal, H. Birnbaum, Science 164 (1969) 181–183.
[50] A. Mizuno, M. Takata, Y. Okada, T. Okuyama, H. Nishino, A. Nishino, J. Takayasu, A. Iwashima, Planta Med. 60 (1994) 333–336.
[51] G. Bryantseva, I.V. Sokolova, A.B. Tsyrenzhapova, N.I. Selivanov, V.P. Khilya, Y.L. Garazd, J. Appl. Spectrosc. 75 (2008) 700–705.
[52] C. Spino, M. Dodier, S. Sotheeswaran, Bioorg. Med. Chem. Lett. 8 (1998) 3475–3478.
[53] F. Cottigli, G. Loy, D. Garau, C. Floris, M. Caus, R. Pompei, L. Bonsignore, Phytomedicine 8 (2001) 302–305.
[54] A.S. Al-Kady, M. Gaber, M.M. Hussein, E.M. Ebeid, J. Phys. Chem. A 113 (2009) 9474–9484.
[55] K.C. Fylaktakidou, D.J. Hadjipavlou-Litina, K.E. Litinas, D.N. Nicolaides, Curr. Pharm. Des. 10 (2004) 3813–3833.
[56] R.O.J. Weinzierl, Mechanisms of Gene Expression, Imperial College Press, London, 1999, Chapter 9.
[57] P.M. Aguirre, J.B. Cacho, L. Folgueira, M. Lopez, J. Garcia, A.C. Velasco, J. Clin. Microbiol. 28 (1990) 148–149.
[58] K.E. Beatty, J.C. Liu, F. Xie, D.C. Dieterich, E.M. Schuman, Q. Wang, D.A. Tirrell, Angew. Chem. Int. Ed. 45 (2006) 7364–7367.
[59] M.Y. Ebeid, K.M. Amin, M.M. Hussein, Egypt. J. Pharm. Sci. 28 (1997) 183–191.
[60] J.M. Thomas, T.A. Clarke, J. Chem. Soc. A (1968) 457–460.
[61] M.J. Pilling, P.W. Seakins, Reaction Kinetics, Oxford University Press, New York, 1995.
[62] M. Katoh, M. Orihara, T. Moriga, I. Nakabayashi, S. Sugiyama, S. Tanaka, J. Solid State Chem. 156 (2001) 225–229.
[63] H.D. Ruan, R.L. Forst, J.T. Kloprogge, L. Duong, Spectrochim. Acta Part A 58 (2002) 967–981.
[64] G.N. Kustova, V.A. Sadykov, S.G. Poryvaev, Phys. Chem. Miner. 18 (1992) 379–382.
[65] J.R. Lakowicz, Principles of Fluorescence Spectroscopy, Plenum Press, New York/London, 1983.
[66] R.M. Melavanki, R.A. Kusanur, J.S. Kadadevaramath, M.V. Kulakarni, J. Lumin. 129 (2009) 1298–1303.
[67] B.G. Evale, S.M. Hanagodimath, J. Lumin. 129 (2009) 1174–1180.
[68] R.M. Melavanki, R.A. Kusanur, M.V. Kulakarni, J.S. Kadadevaramath, J. Lumin. 128 (2008) 573–577.
[69] C. Tablet, M. Hillebrand, J. Photochem. Photobiol. A: Chem. 189 (2007) 73–79.
[70] J.R. Lakowicz, Principles of Fluorescence Spectroscopy, third ed., Springer, New York, 2006, Chapter 8.
[71] T.L. Nemzek, W.R. Ware, J. Chem. Phys. 62 (1975) 477–489.
[72] W.R. Ware, J.S. Novros, J. Chem. Phys. 70 (1966) 3246–3253.
[73] J.M. Frank, S.J. Wawilow, Z. Phys. 69 (1931) 100–110.
[74] J.T. Edward, Molecular Volumes and Parachor, Chem. Ind., London, 1956, p. 774.
[75] J.C. Andre, M. Niclause, W.R. Ware, Chem. Phys. 28 (1978) 371–377.